nature communications

Article

https://doi.org/10.1038/s41467-024-51043-z

Thermo-responsive aqueous two-phase system for two-level compartmentalization

Received: 21 September 2023

Accepted: 26 July 2024

Published online: 08 August 2024

Check for updates

Huanqing Cui[1], Yage Zhang[2,3], Sihan Liu[1], Yang Cao[1], Qingming Ma[4], Yuan Liu[1,2], Haisong Lin[1,2], Chang Li[1], Yang Xiao[1,5], Sammer Ul Hassan[1,2] & Ho Cheung Shum[1,2]

Hierarchical compartmentalization responding to changes in intracellular and extracellular environments is ubiquitous in living eukaryotic cells but remains a formidable task in synthetic systems. Here we report a two-level compartmentalization approach based on a thermo-responsive aqueous two-phase system (TR-ATPS) comprising poly(*N*-isopropylacrylamide) (PNIPAM) and dextran (DEX). Liquid membraneless compartments enriched in PNIPAM are phase-separated from the continuous DEX solution via liquid-liquid phase separation at 25 °C and shrink dramatically with small second-level compartments generated at the interface, resembling the structure of colloidosome, by increasing the temperature to 35 °C. The TR-ATPS can store biomolecules, program the spatial distribution of enzymes, and accelerate the overall biochemical reaction efficiency by nearly 7-fold. The TR-ATPS inspires on-demand, stimulus-triggered spatiotemporal enrichment of biomolecules via two-level compartmentalization, creating opportunities in synthetic biology and biochemical engineering.

Living eukaryotic cells can simultaneously coordinate essential cellular and metabolic events, such as gene expression and enzymatic reactions, by subdividing intracellular space into discrete compartments[1–3]. These compartments of biocomponents within eukaryotic cells can spatiotemporally concentrate and localize reactants or protect unstable intermediates from unfavorable micro-environments in either membrane-bound or membraneless form[4–6]. While canonical organelles, such as mitochondria and the Golgi apparatus, are surrounded by lipid bilayer membranes, the liquid-state membraneless compartments, also known as membraneless organelles, have recently aroused broad interest due to their essential roles in regulating biological functions[7–10], such as stress response[11] and RNA metabolism[12]. Membraneless compartments display high dynamicity and flexibility due to the absence of membrane structure and can fuse upon physical contact and exchange molecules with the surrounding cytoplasm or nucleoplasm[13–17]. They can also be dynamically assembled and dissociated in response to cellular microenvironmental changes[18]. The unique advantages offered by membraneless organelles towards signal transduction, biomolecule storage, and gene expression attracts drastic interest from the science community in designing artificial counterparts. Since the discovery of liquid P granules in the embryo, liquid-liquid phase separation (LLPS) of biomolecules has been recognized as an essential approach to forming membraneless compartments[19–21] and hence been widely adopted in artificial mimics capable of compartmentalization[22–26].

Aqueous two-phase systems (ATPSs) are formed via LLPS, a process of demixing a homogeneous aqueous solution containing two incompatible components into two distinct aqueous phases above a critical concentration or temperature[27–29]. They have emerged as promising in-vitro compartmentalization models owing to their all-water and biocompatible environment[30–32]. The compartmentalization in ATPSs can program the spatial distribution of biomolecules, including

[1]Department of Mechanical Engineering, The University of Hong Kong, Pokfulam Road, Hong Kong (SAR), China. [2]Advanced Biomedical Instrumentation Centre, Hong Kong Science Park, Shatin, New Territories, Hong Kong (SAR), China. [3]School of Biomedical Engineering, Shenzhen University Medical School, Shenzhen University, 518055 Shenzhen, Guangdong, China. [4]School of Pharmacy, Qingdao University, 266071 Qingdao, China. [5]College of Chemistry and Materials Science, Anhui Normal University, Wuhu, Anhui, China. e-mail: ashum@hku.hk

enzymes, polypeptides, RNA, and DNA, through partitioning[33–37]. Despite the significant advances in building systems for compartmentalization based on the emerging ATPSs, regulating hierarchical compartmentalization via external stimuli remains challenging since most reported ATPSs are composed of inert components without stimuli-responsive functions.

In this study, we develop a thermo-responsive ATPS (TR-ATPS) that allows regulating two-level compartmentalization through two-step phase separation. The TR-ATPS comprising thermo-responsive poly(*N*-isopropylacrylamide) (PNIPAM) and dextran (DEX) displays sensitive phase transition behaviors in response to temperature variations. In a PNIPAM (5 wt%)/DEX (5 wt%) solution, liquid membraneless compartments enriched in PNIPAM separate from the continuous DEX-rich phase at 25 °C. When the temperature is increased to 35 °C, the size of PNIPAM compartments decreases sharply from 56–145 μm to 14–60 μm, accompanied by the generation of small second-level compartments (~1 μm) at the interface. The second-step phase separation of the TR-ATPS is thermally reversible, according to the reconfiguration of PNIPAM chains between hydrophilic coils and hydrophobic globules[38–40]. The transition temperature of the TR-ATPS is around 31 °C, close to the human body temperature, rendering the system suitable for investigating biochemical reactions in vitro. As a demonstration, we introduce glucose oxidase and horseradish peroxidase into the TR-ATPS and observe their colocalization in the colloidosome-like compartments when the temperature is increased to 35 °C. The enrichment of enzymes in the small second-level compartments with large surface area accelerates the tandem enzymatic reaction efficiency by approximately 7-fold. This work introduces the concept of TR-ATPS that displays two-level compartmentalization via two-step phase separation in response to temperature changes and regulates biocomponents localization spatiotemporally. The current study provides insights into the development of environment-adaptive compartmentalization systems with potential applications as microreactors and extraction tools beneficial to biochemical process engineering and synthetic biology.

Results

Compartmentalization of TR-ATPS

Thermo-responsive polymer PNIPAM with a number-average molecular weight of 103 kg/mol and a lower critical solution temperature (LCST) of 31.5 °C is adopted as one component of the TR-ATPS to endow the compartmental system with stimuli-responsive functions (Fig. 1a)[41,42]. In a PNIPAM/DEX system composed of 5 wt% PNIPAM and 5 wt% DEX, the repulsive interactions between the incompatible PNIPAM and DEX trigger the formation of micro-droplets enriched in PNIPAM through LLPS at 25 °C[43,44]. When the temperature is increased above the LCST of PNIPAM, e.g., 35 °C, PNIPAM chains reconfigure from hydrophilic coils to hydrophobic globules, triggering the second step of phase separation. The original liquid compartments shrink gradually and disappear due to the insolubilization of PNIPAM above its LCST, generating small compartments stacking at the transient original compartment interface, and forming a colloidosome-like structure. The generated colloidosome-like compartments can store biomolecules (e.g., proteins, polypeptides, and RNA) and regulate enzymatic catalysis speeds via the interception of enzymes (Fig. 1b, c).

To visualize the generated compartments in the TR-ATPS as mentioned above, rhodamine and fluorescein isothiocyanate (FITC) are selected to label PNIPAM and DEX, respectively. Liquid compartments enriched in PNIPAM with diameters ranging from 56 to 145 μm are phase-separated from the continuous DEX phase at 25 °C, as shown in Fig. 2a–g. The separated fluorescence signals of rhodamine and FITC (Fig. 2h) and the rapid coalescence of the PNIPAM droplets within 3 s (Supplementary Fig. 1a and Supplementary Movie 1) indicate that the system undergoes a segregative LLPS. We further characterize the dynamics of the phase-separated droplet by fluorescence recovery after photobleaching (FRAP) measurements. A phase-separated compartment enriched in PNIPAM is observed at 25 °C, as shown in Supplementary Fig. 2a. The fluorescence intensity in the bleached region recovers to 92% of the initial intensity within 15 s (Supplementary Fig. 2b–d). The 92% intensity recovery indicates the free diffusion of fluorescent molecules and thus confirms the liquid-like state of the phase-separated membraneless compartment. When the temperature is increased to 35 °C, the diameters of the primary compartments decrease from 56–145 μm to 14–60 μm (Fig. 2i–o). During the heating process, small second-level compartments (~1 μm) enriched in PNIPAM are generated at the interface of the primary compartments, accompanied by the migration of DEX from the continuous phase to the phase-separated second-level compartments (Fig. 2l–n). PNIPAM and DEX undergo interfacial co-precipitation, similar to the interfacial polyelectrolyte complexation[45,46]. PNIPAM is not dissolved in water when the temperature is higher than its LCST. The formed interfacial second-level compartments display solid-like properties as confirmed by the stable interface without coalescence (Supplementary Fig. 1b and Supplementary Movie 2) and the larger elastic modulus than the viscous modulus at 35 °C (Supplementary Fig. 3). These small second-level compartments display the characteristics of "colloidal particles"[47]. The outer phase is mainly water with little DEX dissolved (Supplementary Fig. 4). The small compartments located at the interface consist of physically associated PNIPAM and DEX. The inner phase of large compartments is mainly water. Both phenomena can be attributed to the reconfiguration of PNIPAM chains from hydrophilic coils to hydrophobic globules in response to temperature changes[48]. The overlap of fluorescence signals of rhodamine and FITC, as shown in Fig. 2p, implies the colocalization of PNIPAM and DEX. Small second-level compartments consisting of PNIPAM and DEX are observed on the surface of the primary compartment at 35 °C, as shown in Fig. 2q–s. Small second-level compartments are merely located at the edge, as indicated by the fluorescent interface and the dark core of the cross-section of the primary compartment (Fig. 2t–v). The z-stack confocal images (Fig. 2w and Supplementary Movie 3) demonstrate the compartment's three-dimensional (3D) structure—small second-level compartments self-assemble at the interface of the primary compartment, resembling colloidosomes in appearance. The size of the small second-level compartment is associated with the molecular weight of PNIPAM and the size of the primary compartment. The PNIPAM is synthesized by traditional radical polymerization with a polydispersity index of 1.59 (Supplementary Fig. 5). The broad molecular weight distribution indicates the different lengths of PNIPAM chains. When the temperature is above the LCST, PNIPAM chains with different lengths aggregate to form small second-level compartments with varying sizes at the interface of a primary compartment (Supplementary Fig. 6a). To confirm whether the size of the second-level compartment is associated with the size of the primary compartment, we decrease the size of primary compartments from 56–145 μm to 25–80 μm via extending vortex time. When the temperature is increased to 35 °C, the average size of generated second-level compartments decreases from ~1 μm to ~235 nm (Supplementary Fig. 6b). These results indicate that it is convenient to modulate the size of small second-level compartments by changing the diameter of primary compartments.

Thermally reversible compartmentalization of TR-ATPS

The phase-separated PNIPAM droplets generated by directly mixing PNIPAM and DEX at 25 °C coalesce over time. The phase separation would eventually reach equilibrium, forming two phases with a clear interface. To better demonstrate the thermo-reversible properties of TR-ATPS, we use microfluidics to generate stabilized all-aqueous double emulsions in oil. The incorporation of surfactant in the oil phase prevents the coalescence of all-aqueous double emulsions, convenient for observing the thermally reversible compartmentalization of TR-ATPS. The TR-ATPS composed of 5 wt% PNIPAM and 5 wt%

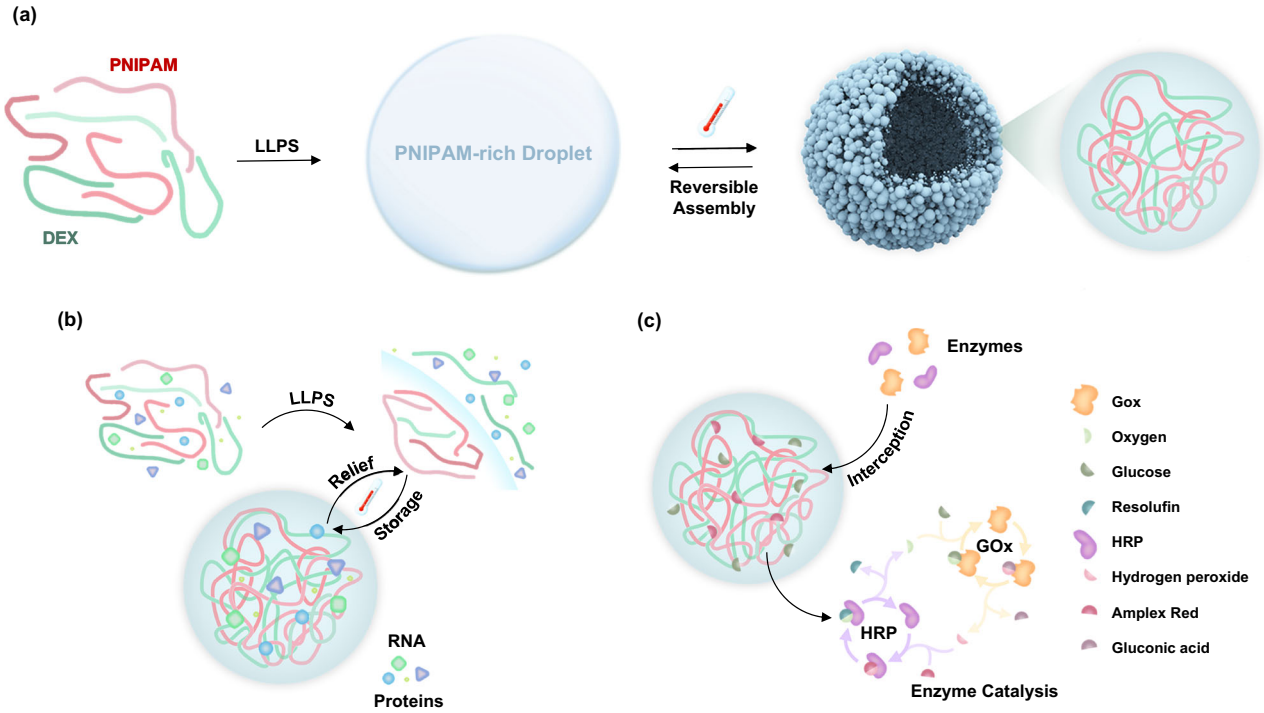

Fig. 1 | Schematic of two-level compartmentalization of TR-ATPS. a Schematics of two-level compartmentalization of the PNIPAM/DEX system. **b** Biomolecular storage and (**c**) enzyme cascade reaction in the colloidosome-like compartments.

DEX would reach equilibrium by phase separating into a PNIPAM-rich phase and a DEX-rich phase, which are then selected as the external and the internal phases, respectively, to generate all-aqueous double emulsions using droplet microfluidics (Fig. 3a). The continuous flow of the two phases is sheared by an oil phase consisting of FC-40 with 1% fluorosurfactant. The generated all-aqueous emulsions with DEX-rich cores and PNIPAM-rich shells (Fig. 3b) are collected and sealed in a chamber to avoid evaporation. By labeling DEX and PNIPAM with FITC and rhodamine, respectively, all-aqueous double emulsions with green cores of 46 ± 9 μm (Fig. 3c and Supplementary Fig. 7a) and red shells of 15 ± 5 μm (Fig. 3d and Supplementary Fig. 7b) are observed at 25 °C. The separated fluorescence signals with clear interfaces (Fig. 3e, f) imply the PNIPAM/DEX system undergoes segregative LLPS at 25 °C. As the temperature increases to 35 °C, the thickness of shells decreases by around 30%, accompanied by the migration of green fluorescence signals from the cores to the shells, leaving dark cores (Fig. 3g–i and Supplementary Fig. 7c). Small second-level compartments composed of hydrophobic PNIPAM aggregates are generated at the interface of the primary compartment triggered by thermo-induced coil-to-globule transition of PNIPAM chains, resembling the colloidosome-like structure observed in the non-equilibrium state. The overlap of fluorescence signals of FITC and rhodamine (Fig. 3i, j) implies that PNIPAM and DEX colocalize in the generated second-level compartments at 35 °C.

To visualize the transition dynamics, the changes in fluorescence signals during the heating process are simultaneously recorded by a confocal microscope (Supplementary Movie 4). Red shells consisting of the PNIPAM-rich phase shrink first and the size of shells decreases from 8–24 μm to 7–16 μm within 34 s, while no noticeable change occurs in the green shells of the DEX-rich phase. The green fluorescence signal of the DEX-rich phase starts to migrate to the red signals of PNIPAM-rich shells at 51 s and completely overlaps with the red signal within 68 s. The shells thin out to 6–15 μm during this period. Phase transition reaches equilibrium at 68 s as heating for over 68 s does not trigger other noticeable variations of the size and the fluorescence signals of all-aqueous double emulsions. The phase transition of the equilibrated TR-ATPS is thermally reversible, verified by recording the variations of fluorescence signals during the subsequent cooling (Supplementary Movie 5). As the temperature decreases from 35 °C to 25 °C, green FITC and red rhodamine signals start to separate at 17 s, completely isolated after 51 s, and reach the final stable core-shell structure after 204 s. The recovery of the initially separated FITC and rhodamine signals along a decreasing temperature confirms the phase transition of the PNIPAM/DEX system is thermally reversible.

Mechanism of two-level compartmentalization

The underlying principle of two-level compartmentalization is the repulsive interactions between the incompatible polymers and the thermally reversible reconfiguration of PNIPAM chains. When the temperature is below the LCST of PNIPAM, i.e., 25 °C, PNIPAM chains present the configuration of hydrophilic coils[42]. Hydrogen bonds are formed between the amide groups of PNIPAM and water molecules, and between the hydroxyl groups of DEX and water molecules, respectively (Fig. 4a)[49,50]. As the concentration of the ATPSs containing PNIPAM is above the binodal curve, the repulsive interactions between the incompatible PNIPAM and DEX trigger the first level of compartmentalization by forming membraneless compartments enriched in PNIPAM[44,48]. Increasing the temperature above the LCST of PNIPAM, i.e., 35 °C, induces the reconfiguration of PNIPAM chains from hydrophilic coils to hydrophobic globules[48], breaking the formed hydrated layer on the PNIPAM chains. PNIPAM contains amide groups (-CONH-) that can act as hydrogen bond acceptors, while DEX contains hydroxyl groups (-OH) that can act as hydrogen bond donors[51,52]. Hydrogen bonds subsequently rearrange between the amide groups of hydrophobic PNIPAM globules and the hydroxyl groups of DEX. The formation of hydrogen bonds can lead to the physical association of PNIPAM and DEX. The reconfiguration of PNIPAM chains in response to temperature changes induces the dramatic shrinkage of the primary compartments, accompanied by the generation of small second-level compartments at the interface. To verify our hypothesis, attenuated total reflectance Fourier transform infrared spectroscopy (ATR-FTIR) of the PNIPAM (5 wt%)/DEX (5 wt%) aqueous solution below and above

https://doi.org/10.1038/s41467-024-51043-z

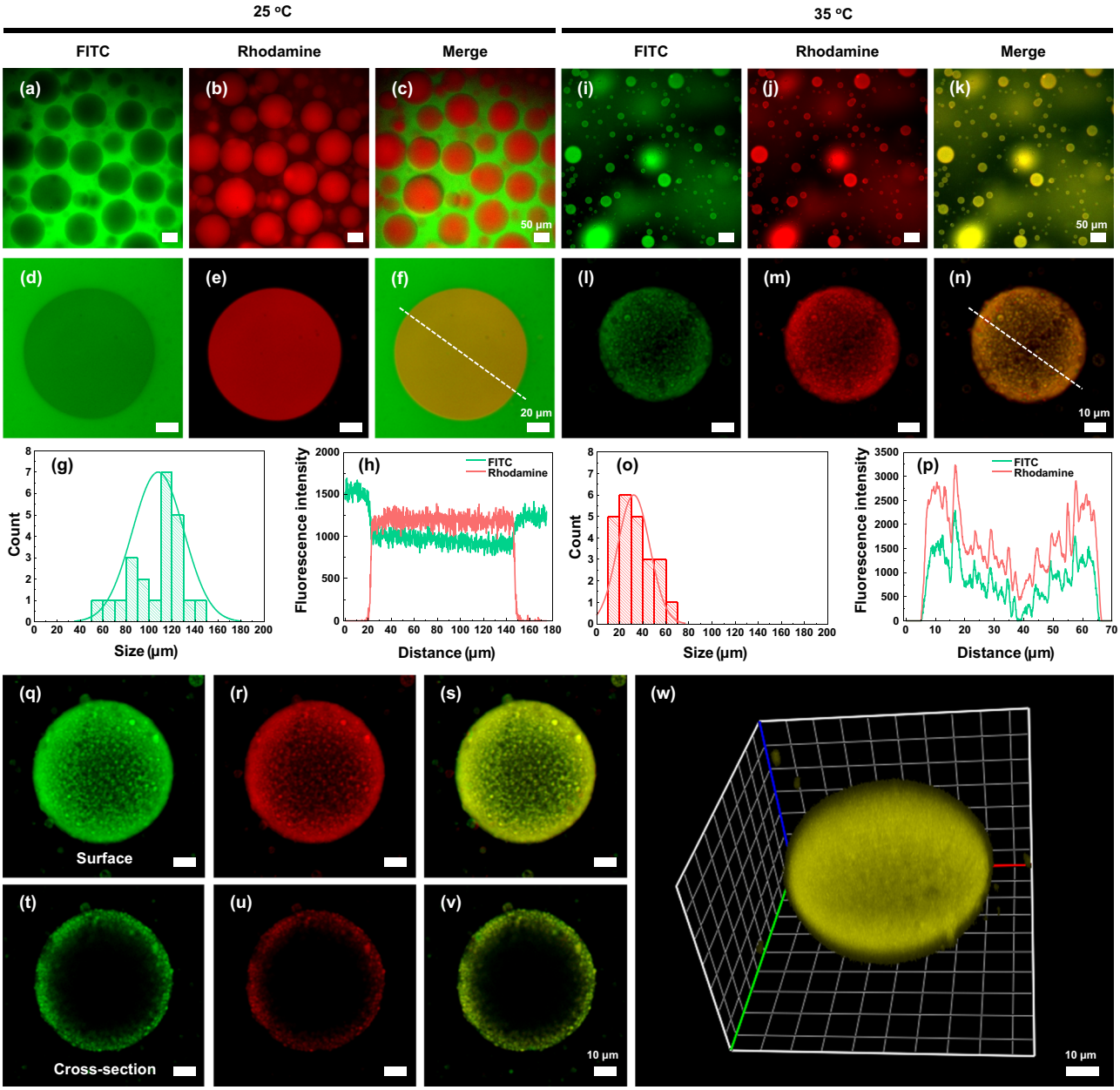

Fig. 2 | Compartmentalization of the PNIPAM/DEX system at different temperatures. Phase-separated PNIPAM droplets in PNIPAM (5 wt%)/DEX (5 wt%) solution under (**a**) FITC channel, (**b**) rhodamine channel, and (**c**) merged channel at 25 °C. Confocal images of PNIPAM droplets in PNIPAM (5 wt%)/DEX (5 wt%) solution under (**d**) FITC channel, (**e**) rhodamine channel, and (**f**) merged channel at 25 °C. **g** Histogram illustrating the size distribution of primary compartments at 25 °C. Results are collected from more than $n > 20$ different primary compartments. **h** The fluorescence intensity profile shows the distribution of PNIPAM and DEX along the white dash line in (**f**). Phase-separated PNIPAM droplets in PNIPAM (5 wt%)/DEX (5 wt%) solution under (**i**) FITC channel, (**j**) rhodamine channel, and (**k**) merged channel at 35 °C. Confocal images of PNIPAM droplets in PNIPAM (5 wt%)/DEX (5 wt%) solution under (**l**) FITC channel, (**m**) rhodamine channel, and (**n**) merged channel at 35 °C. **o** Histogram illustrating the size distribution of primary compartments at 35 °C. Results are collected from more than $n > 20$ different primary compartments. **p** The fluorescence intensity profile shows the distribution of PNIPAM and DEX along the white dash line in (**n**). Confocal images show the colloidosome-like surface structure under (**q**) FITC channel, (**r**) rhodamine channel, and (**s**) merged channel. The cross-section of the hierarchical multi-compartment under (**t**) FITC channel, (**u**) rhodamine channel, and (**v**) merged channel. Z-stack confocal images of colloidosome-like compartments formed in the PNIPAM (5 wt%)/DEX (5 wt%) system under (**w**) merged channel.

the LCST of PNIPAM was recorded. The sharp absorption peak around 3600 cm^{-1} shown in Fig. 4b is assigned to the stretching vibration of free OH groups of DEX[53]. When the temperature is increased above the LCST of PNIPAM, the sharp absorption peak around 3600 cm^{-1} disappears into a broad absorption peak ranging from 3500 cm^{-1} to 3200 cm^{-1}. The broad absorption peak should belong to the intermolecular hydrogen bond O-H stretching vibration between PNIPAM and DEX[54]. To further confirm our hypothesis, ^{1}H nuclear magnetic resonance (^{1}H-NMR) spectroscopy of the 5 wt% PNIPAM, 5 wt% DEX, and PNIPAM (5 wt%)/DEX (5 wt%) aqueous solution at 25 °C and 35 °C using D_2O as the solvent, are recorded, as shown in Fig. 4c. The peaks located at 3.5–4.0 ppm and 5 ppm belong to DEX, while those at 1.16, 1.59, 2.02, and 3.89 ppm are assigned to PNIPAM[55]. When the temperature is increased from 25 to 35 °C, the characteristic peaks of PNIPAM located at 1.59 ppm and 2.02 ppm disappear, and the peak located at 1.16 ppm at 25 °C shifts to 1.27 ppm with significantly reduced intensity. The reconfiguration of PNIPAM chains breaks the formed hydrogen between the amide groups of PNIPAM and water

https://doi.org/10.1038/s41467-024-51043-z

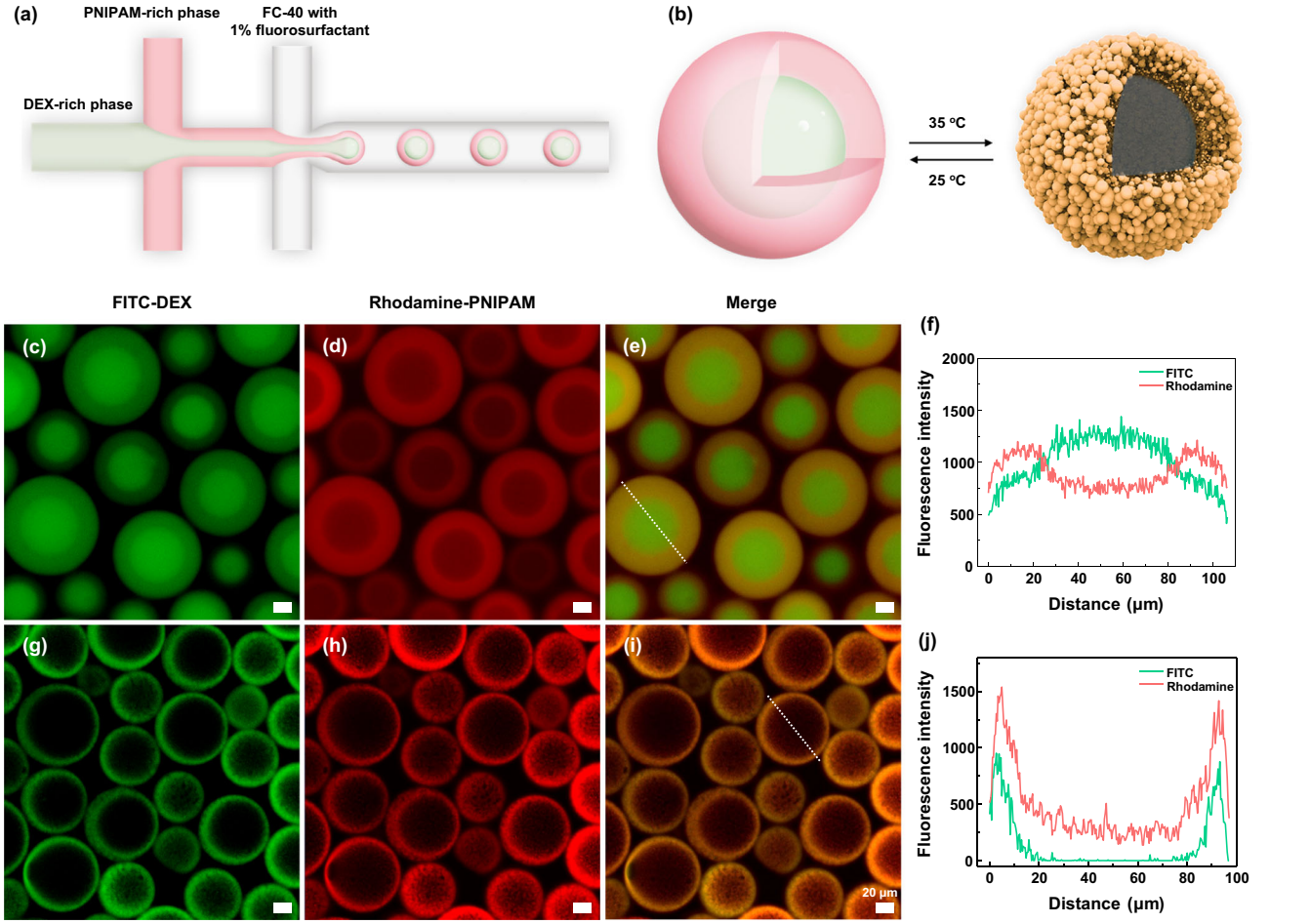

Fig. 3 | Thermally reversible two-level compartmentalization of the PNIPAM/DEX system at different temperatures. a Schematic illustration of generating PNIPAM/DEX all-aqueous double emulsions by droplet microfluidics. **b** Schematic diagram displaying the phase transition in the resulting all-aqueous double emulsions. All-aqueous double emulsions with dex-rich cores and PNIPAM-rich shells under (**c**) FITC channel, (**d**) rhodamine channel, and (**e**) merged channel at 25 °C. Each experiment was repeated independently three times with similar results. **f** Fluorescence intensity profile shows the distribution of PNIPAM and DEX along with the white dash line in (**e**). The transition of all-aqueous double emulsions to condensed shells with diluted cores under (**g**) FITC channel, (**h**) rhodamine channel, and (**i**) merged channel at 35 °C. Each experiment was repeated independently three times with similar results. **j** Fluorescence intensity profile shows the distribution of PNIPAM and DEX along with the white dash line in (**i**).

molecules, resulting in the disappearance and shift of the characteristic peaks of PNIPAM. During the heating process, the characteristic peaks of DEX located at 3.5–4.0 ppm and 5 ppm shift to 3.6–4.1 ppm and 5.1 ppm. This indicates that the reconfiguration of PNIPAM chains also has an impact on the formed hydrogen bond between DEX and water due to the physical association with PNIPAM and DEX. All the evidence based on the observed transitions in the ATR-FTIR and H-NMR spectra supports our hypothesis. To confirm the essential role of PNIPAM in the two-level compartmentalization, PNIPAM/polyacrylamide (PAM) has been selected as the positive control. By labeling PNIPAM and PAM with rhodamine and FITC, respectively, the system comprising 5 wt% PNIPAM and 5 wt% PAM displays phase-separated PNIPAM droplets (55–105 μm) from the continuous PAM phase (Fig. 4d) at 25 °C. The repulsive interactions between PNIPAM and PAM drive the first level of compartmentalization. When the temperature is increased to 35 °C (Fig. 4d), the diameter of the primary PNIPAM compartments shrinks to 34–57 μm, accompanied by the generation of small second-level compartments at the surface. This phenomenon is similar to that observed in the PNIPAM/DEX system. An ATPS comprising polyethylene glycol (PEG) and DEX, in which neither two components are thermo-responsive, is selected as another negative control. By labeling PEG and DEX with rhodamine and FITC, respectively, a system comprising 1 wt% PEG and 9 wt% DEX displays phase-separated PEG droplets from the continuous DEX phase (Fig. 4e) at 25 °C. The repulsive forces between the incompatible PEG and DEX drive the phase separation, as reported previously[32]. When the temperature is increased to 35 °C, the phase-separated PEG droplets remain stable without noticeable shape change, as shown in Fig. 4e. The stable compartments with separated fluorescence signals at 35 °C indicate that the lack of stimuli-responsive reconfiguration of polymer chains cannot regulate two-level compartmentalization via external stimulation.

Storage of biomolecules in TR-ATPS

To demonstrate the biomolecular storage function of TR-ATPS, which involves diverse bioactive molecules, fluorescein amidite (FAM) labeled RNA (homopolymer poly(rA) of 40 nt) is selected as the guest biomolecule and mixed with PNIPAM (5 wt%)/DEX (5 wt%) aqueous solution (Fig. 5a). The FAM-RNA displays higher distribution in the more hydrophilic DEX-rich phase at 25 °C, as shown in Fig. 5b. Raising the temperature to 35 °C triggers the second-level compartmentalization, forming the colloidosome-like structures. FAM-RNA migrates into the phase-separated small second-level compartments, as confirmed by Fig. 5b. FAM-RNA is stored in the small compartments. As the temperature recovers to 25 °C, the stored FAM-RNA are released and partitioned into the DEX-rich phase. Except for RNA, proteins and

https://doi.org/10.1038/s41467-024-51043-z

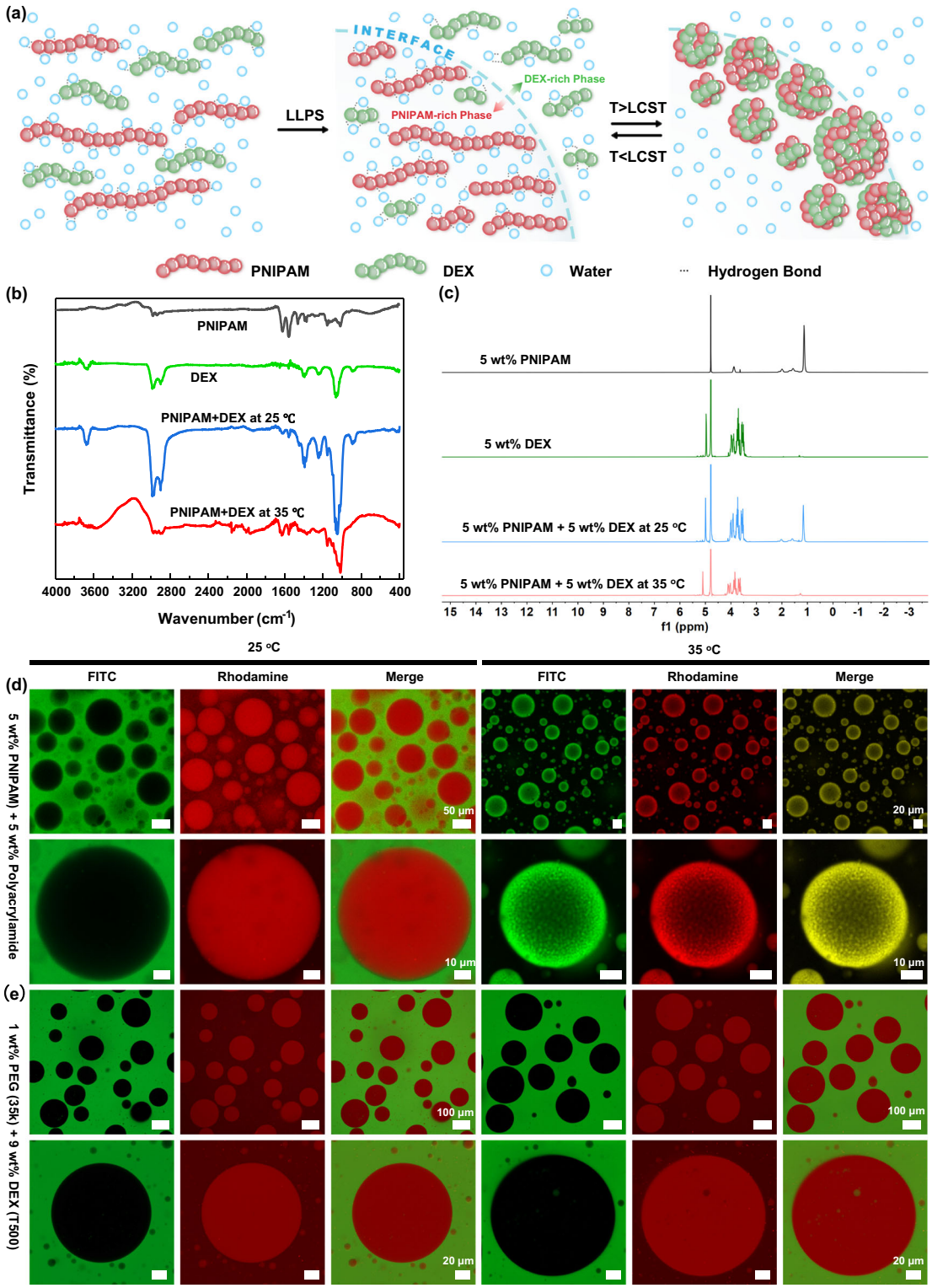

Fig. 4 | Mechanism of two-level compartmentalization. a Schematic of two-level compartmentalization. **b** ATR-FTIR spectra of the PNIPAM (5 wt%)/DEX (5 wt%) aqueous solution at 25 °C and 35 °C. **c** ^{1}H-NMR spectroscopy of the 5 wt% PNIPAM, 5 wt% DEX, and PNIPAM (5 wt%)/DEX (5 wt%) aqueous solution at 25 and 35 °C. **d** Phase-separated PNIPAM droplets in PNIPAM (5 wt%)/PAM (5 wt%) solution under FITC channel, rhodamine channel, and merged channel at 25 and 35 °C. Each experiment was repeated independently three times with similar results. **e** Phase-separated PEG droplets in PEG (1 wt%)/DEX (9 wt%) solution under FITC channel, rhodamine channel, and merged channel at 25 and 35 °C. Each experiment was repeated independently three times with similar results.

polypeptides, such as bull serum albumin (BSA) and poly-L-lysine (PLL), can also be stored and released by the TR-ATPS (Supplementary Fig. 8). The storage and release of biomolecules could be accounted for as follows: When the temperature is above the LCST of PNIPAM, hydrogen bonds subsequently rearrange between the amide groups of hydrophobic PNIPAM globules and the hydroxyl groups of DEX. The formation of hydrogen bonds can lead to the physical association of PNIPAM and DEX. Due to the colocalization of PNIPAM and DEX, biomacromolecules migrate with DEX into the small compartments at the interface due to their strong affinity for DEX[4].

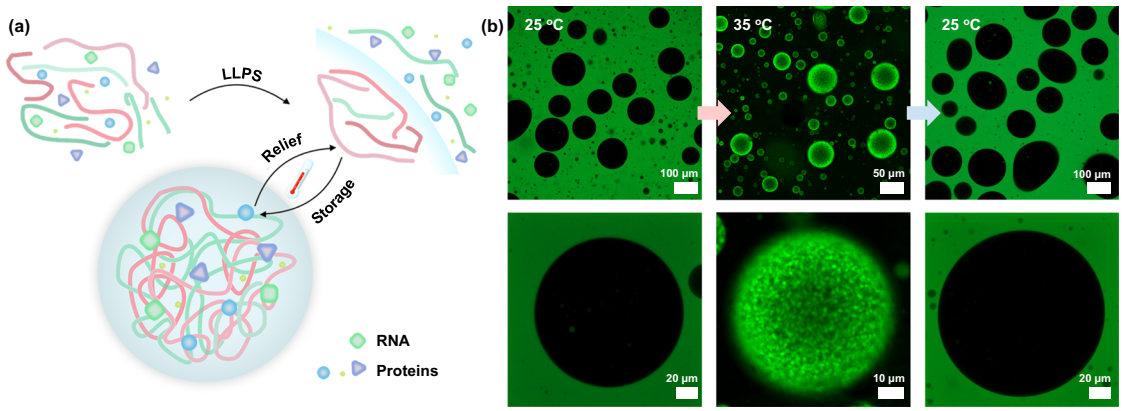

Fig. 5 | Biomolecular storage in TR-ATPS. a Schematic of biomolecules storage in TR-ATPS. Storage and release of (**b**) FAM-RNA in PNIPAM (5 wt%)/DEX (5 wt%) aqueous solution at 35 and 25 °C. Each experiment was repeated independently three times with similar results.

Spatiotemporal regulation of biochemical reaction via two-level compartmentalization

We use a classic bi-enzymatic cascade reaction catalyzed by horseradish peroxidase (HRP) and glucose oxidase (GOX) to demonstrate the regulation of biochemical reactions via two-level compartmentalization. The schematic diagram (Fig. 6a) shows that glucose is converted into gluconic acid and hydrogen peroxide via an oxidation reaction catalyzed by GOX. The resulting H_2O_2 then reacts with amplex red under the mediation of HRP, producing a fluorescent molecule, resorufin, which has a maximum excitation wavelength of 563 nm and emission wavelength of 587 nm[56]. The hydrophilic substrate, glucose, prefers to partition into the more hydrophilic DEX-rich phase, while the hydrophobic substrate, amplex red, partitions into the relatively hydrophobic PNIPAM-rich phase[57]. Rhodamine and FITC are selected to label GOX and HRP to mark their localization in the PNIPAM (5 wt%)/DEX (5 wt%) system. Both rhodamine-labeled GOX and FITC-HRP exhibit uneven spatial distribution between the two phases, as shown in Supplementary Fig. 9a–c. Rhodamine-labeled GOX prefers PNIPAM-rich compartments, and FITC-HRP distributes more in the continuous DEX-rich phase, indicating that GOX and HRP preferentially partition into PNIPAM-rich and DEX-rich phases, respectively (Supplementary Fig. 9d). By raising the temperature to 35 °C, the compartments enriched in PNIPAM dramatically shrink from 35–97 μm to 14–43 μm in diameter (Supplementary Fig. 9e and Supplementary Fig. 10). The rhodamine signal in PNIPAM-rich compartments is approximately 6.5 times stronger than that at 25 °C (Supplementary Fig. 11), implying a 6.5-fold elevation of GOX concentration. During the heating process, HRP migrates from the continuous DEX-rich phase to the shrunk compartments with a 3-fold increment of concentration (Supplementary Fig. 9e–g and Supplementary Fig. 12), achieving the colocalization of GOX and HRP in the interfacial small second-level compartments (Fig. 6b–f). To quantify the preference distribution of enzymes in the presented TR-ATPSs at 25 °C and 35 °C, we measure the partitioning fraction for both GOX and HRP, defined as the fluorescence intensity of each enzyme in the PNIPAM/DEX phase divided by its overall fluorescence intensity, in multiple PNIPAM/DEX systems[58]. The ratios of PNIPAM and DEX are adjusted but the total content of the two is maintained at 10 wt% for the selected PNIPAM/DEX systems. The partitioning fraction of GOX in the compartments enriched in PNIPAM from the PNIPAM (5 wt%)/DEX (5 wt%) system at 25 °C is around 62% (Fig. 6g and Supplementary Fig. 9d), while HRP in the compartments enriched in DEX and PNIPAM is around 55% and 45%, respectively (Fig. 6h, i). Once the temperature increases to 35 °C, the partitioning fraction of GOX and HRP in the interfacial second-level compartments enriched both PNIPAM and DEX dramatically increase to 89% and 68%, respectively (Fig. 6i and Supplementary Fig. 9h). When the mass fraction of DEX increases from 5 wt% to 8 wt%, the partitioning fraction of HRP in the DEX-rich phase slightly rises from 55% to 60%, while GOX in PNIPAM decreases from 62% to 54% (Fig. 6g–i and Supplementary Figs. 13–15). By raising the temperature from 25 °C to 35 °C, the partitioning fraction of GOX and HRP in the interfacial small second-level compartments drops to 74% and 58%, respectively. These results indicate that PNIPAM dominates the colocalization of GOX and HRP. The significant difference in the partitioning fraction of both enzymes implies that the localization of biocomponents can be regulated via compartmentalization of the PNIPAM/DEX system stimulated by temperature variations and/or the components of the system.

To evaluate the catalytic efficiency of GOX and HRP, we measure the fluorescence intensity of resorufin generated from the tandem enzymatic reactions. No resorufin is produced in the absence of GOX and HRP due to the lack of catalysts, as confirmed by Supplementary Fig. 16a, b. Resorufin is generated under the catalysis of GOX and HRP and prefers to partition into PNIPAM-rich compartments (Supplementary Fig. 16c, d). The partitioning fraction of resorufin in the compartments increases from 58% to 80% when the temperature has risen from 25 °C to 35 °C (Supplementary Fig. 16e). To confirm the impact of temperature on the fluorescence intensity of resorufin, the fluorescence signals of resorufin (125 μM) in 1X buffer solutions (50 mM sodium phosphate buffer, pH 7.4) are monitored at 25 and 35 °C. When the temperature is raised from 25 to 35 °C, the intensity varies by less than 5 % (Supplementary Fig. 17a), indicating that temperature has only negligible influence on the resorufin intensity. To verify the influence of the local environment of the fluorophore on its fluorescence intensity, we record the intensity of 125 μM resorufin in different working solutions. Compared with resorufin in 1X buffer solution, the fluorescence intensity decreases by 11 % and 41 % in 5 wt% PEG and 5 wt% DEX, respectively, but increases by 53% in 5 wt% PNIPAM (Supplementary Fig. 17b). These results imply that the local environment has a significant impact on the intensity of resorufin. The variance of fluorescence intensity can be explained by the hydrophobic nature of resorufin, which tends to adopt a more stable and relaxed conformation in relatively hydrophobic macromolecular crowding surroundings than in hydrophilic polymer solutions. It allows for more efficient energy transfer between excited and ground states, resulting in higher fluorescence intensity. To study the impact of turbidity associated with the presence of droplets, the intensities of 125 μM resorufin in two ATPSs are also recorded for comparison. The intensity of resorufin decreases by 26.5 % in a PEG (1 wt%)/DEX (9 wt%) solution, while it rises by 29 % in a PNIPAM (5 wt%)/DEX (5 wt%) solution (Supplementary Fig. 17b). The turbidity associated with the presence of droplets slightly improves the intensity in comparison with that in a single-phase solution, probably due to the compartmentalization-induced enrichment of resorufin. To avoid the impact of the local environment on the intensity of resorufin, the standard curves of resorufin in a 50 mM sodium phosphate buffer, a 50 mM

https://doi.org/10.1038/s41467-024-51043-z

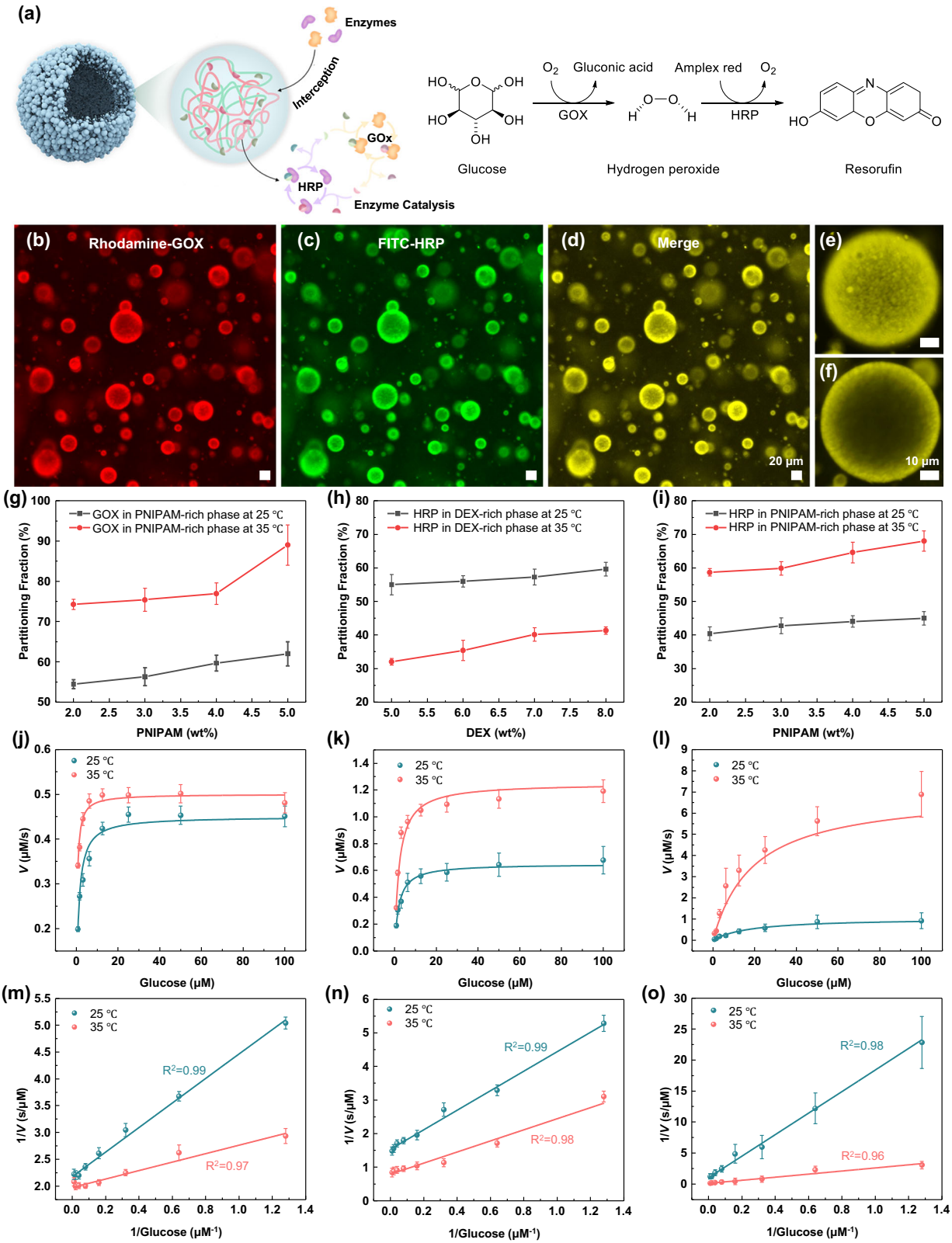

sodium phosphate buffer solution containing 1 wt% PEG and 9 wt% DEX, and a 50 mM sodium phosphate buffer solution containing 5 wt% PNIPAM and 5 wt% DEX are calibrated (Supplementary Fig. 18). The intensity of resorufin shows a good linear relationship with its concentration in all these solutions.

To quantify the catalytic efficiency, the kinetic behaviors of GOX@HRP in different working solutions are investigated by monitoring the fluorescence of the oxidation product of amplex red in 1-min intervals while changing the concentration of substrate, glucose. The oxidation product of amplex red catalyzed by GOX@HRP shows a time-dependent linear increase after the addition of glucose, as shown in Supplementary Fig. 19. A detailed kinetic analysis of GOX@HRP in these working solutions is demonstrated in Fig. 6j–l. The initial reaction rate versus the concentration of glucose follows the typical

Fig. 6 | Spatiotemporal regulation of bi-enzymatic cascade reactions through compartmentalization of GOX and HRP in PNIPAM/DEX systems. a Schematic diagram and chemical reaction equations demonstrating the generation of resorufin catalyzed by GOX and HRP. Colocalization of GOX and HRP in the small second-level compartments from the PNIPAM (5 wt%)/DEX (5 wt%) under (**b**) rhodamine channel, (**c**) FITC channel, and (**d**) merged channel at 35 °C. The confocal images show the colocalization of GOX and HRP on the (**e**) surface and (**f**) cross-section of the colloidosome-like compartments under the merged channel at 35 °C. **g** Partitioning fraction of GOX in PNIPAM-rich phase from PNIPAM/DEX systems at 25 °C and 35 °C. **h** Partitioning fraction of HRP in DEX-rich phase from PNIPAM/DEX systems at 25 °C and 35 °C. **i** Partitioning fraction of HRP in PNIPAM-rich phase from PNIPAM/DEX systems at 25 °C and 35 °C. Michaelis–Menten plots of tandem reactions catalyzed by GOX and HRP in (**j**) a 50 mM sodium phosphate buffer (pH 7.4), (**k**) a 50 mM sodium phosphate buffer (pH 7.4) containing PEG (1 wt%)/DEX (9 wt%), and (**l**) a 50 mM sodium phosphate buffer (pH 7.4) containing PNIPAM (5 wt%)/DEX (5 wt%) at 25 and 35 °C. Lineweaver–Burk plots of tandem reactions catalyzed by GOX and HRP in (**m**) a 50 mM sodium phosphate buffer (pH 7.4), (**n**) a 50 mM sodium phosphate buffer (pH 7.4) containing PEG (1 wt%)/DEX (9 wt%), and (**o**) a 50 mM sodium phosphate buffer (pH 7.4) containing PNIPAM (5 wt%)/DEX (5 wt%) at 25 and 35 °C. Error bars indicate mean ± SD (n = 3 independent samples).

Michaelis–Menten kinetics. The maximum initial velocity (V_{max}) of GOX@HRP in different working solutions is calculated based on the Lineweaver–Burk plots (Fig. 6n, o and Supplementary Table 1). A significantly enhanced V_{max} of GOX@HRP from 1.101 to 6.638 μM/s is observed in a 50 mM sodium phosphate buffer (pH 7.4) containing PNIPAM (5 wt%)/DEX (5 wt%), when the temperature is raised from 25 to 35 °C. The K_m value of GOX/HRP increases from 1.339 μM in 1x buffer to 3.165 μM in PNIPAM (5 wt%)/DEX(5 wt%) at 25 °C. The variation in the K_m is probably induced by the hydrophilicity of the environment[59]. The V_{max}/K_m values are similar in the three working solutions at 25 °C, indicating their comparable catalytic efficiency. When the temperature is increased from 25 to 35 °C, The K_m values decrease in all three working solutions, indicating the higher affinity between enzymes and substrates. Raising temperature increases the kinetic energy of molecules, resulting in more frequent and energetic collisions between the enzyme and substrate[60]. Raising the temperature increases the V_{max}/K_m values in the three working solutions. The V_{max}/K_m values in PNIPAM (5 wt%)/DEX (5 wt%) solutions increase from 0.348 to 2.495 s^{-1}, implying that the overall reaction efficiency is improved by around 7-fold. To verify the influence of temperature on the activities of the enzymes, we use the glucose oxidase assay kit and peroxidase assay kit from ThermoFisher to quantify the enzymatic activities. The standard curve of glucose oxidase and HRP shows a good linear relationship with the fluorescence intensity of the product (resorufin), as shown in Supplementary Fig. 20. When the temperature is increased from 25 to 35 °C, the activities decrease by 7 %-15 % for glucose oxidase, and ~5.5 % for HRP. The 1.13-fold enhanced V_{max} in the buffer solution is probably induced by the faster diffusion of components. To verify the essential role of the thermo-responsive phase separation in expediting enzymatic reaction rates, a PEG/DEX system has been selected as a control since neither PEG nor DEX displays reconfiguration in response to temperature changes. A 2-fold enhanced V_{max} was observed in a 50 mM sodium phosphate buffer (pH 7.4) containing 1 wt% PEG and 9 wt% DEX. Utilizing fluorescence dye Rhodamine and FITC to label GOX and HRP, respectively, enzymes show no alternation in the PEG/DEX system during the heating process, as confirmed by Supplementary Fig. 21, 22. The improved V_{max} in the PEG/DEX system may be due to the macromolecular crowding environment and faster diffusion of molecules[61,62]. The 7-fold improvement of the overall reaction efficiency in the TR-ATPS is probably due to the generation of small compartments via two-level compartmentalization, which produces a higher specific surface area and enriches enzymes in the small compartments. The faster diffusion of components and the variation of the local environment may also play a role in such a process. The TR-ATPS, capable of spatiotemporally regulating biocomponents via compartmentalization in response to external stimuli, would provide insights into developing synthetic cells with hierarchical structures and cell-mimetic functions.

Discussion

In summary, this work introduces TR-ATPSs using the PNIPAM/DEX system as the delegate. TR-ATPSs display two-level compartmentalization in response to temperature changes. For the PNIPAM/DEX system, PNIPAM-enriched liquid membraneless compartments are separated from the continuous DEX phase through LLPS at 25 °C. By raising the temperature to 35 °C, the PNIPAM-rich compartments shrink significantly, accompanied by the generation of small second-level compartments at the interface, resembling colloidosomes in appearance. The underlying principle of two-level compartmentalization is the repulsive interactions between the incompatible polymers and the reconfiguration of PNIPAM chains responding to temperature variations. The generated colloidosome-like compartments can store biomolecules (e.g., proteins, polypeptides, and RNA), effectively program the spatial distribution of enzymes and accelerate tandem enzymatic reaction efficiency by around 7-fold. The TR-ATPSs capable of programming the distribution of biomolecules have the potential to enrich target biomarkers, facilitating rapid and point-of-care diagnosis. The TR-ATPSs display thermally reconfigurable structures between emulsion droplets and colloidosomes in a controllable manner. The unique feature has rarely been reported in artificial systems[63,64]. ATPSs form two immiscible liquid phases that can be easily separated based on their different densities, allowing for efficient recovery of the encapsulated biomolecules. Besides, combining the advantages of aqueous two-phase systems with thermally reconfigurable features presents a unique system design that has not been extensively explored. This approach offers opportunities for the development of innovative enzyme-based technologies and applications. Compared with previously reported ATPSs compartmentalization methods, such as osmosis-driven and evaporation-driven phase separation of a single-phase ATPS droplet[32,36], the compartmentalization of TR-ATPSs controlled by varying the temperature is more reconfigurable and controllable. In particular, unlike the inactivation of biomolecules caused by the complete evaporation of single-phase ATPS droplets or high osmolarity conditions, the temperature-regulated feature renders TR-ATPSs higher biocompatibility under biomolecules-involved scenarios by keeping them in mild aqueous environment.

The concept of TR-ATPS should be applicable to ATPSs containing other thermo-responsive polymers[65,66], which display similar LCST-type phase transition with PNIPAM, such as poly(*N, N*-diethylacrylamide) (PDEA)[67,68]. PDEA displays coil-to-globule phase transition at around 29.5 °C (Supplementary Fig. 23) and can form TR-ATPSs with DEX, PVA, and PAM. The PDEA-based TR-ATPSs display similar two-level compartmentalization via two-step phase separation (Supplementary Fig. 24), proving the university of the TR-ATPS concept. In addition, the LCST of thermo-responsive polymers can be precisely regulated via copolymerization with hydrophilic or hydrophobic comonomers[69]. For instance, copolymers of dimethyl or di-*n*-propyl vinylphosphonate and diethyl vinylphosphonate show tunable LCST between 5 °C and 92 °C[70], which would broaden the application scenarios of TR-ATPSs. Moreover, the approach illustrated by TR-ATPSs may be extended to the design of other types of stimuli-responsive ATPSs, including pH-responsive ATPSs, light-responsive ATPSs, and multiple-responsive ATPSs. For instance, selecting azobenzene-contained polymers as one component can prepare light-responsive ATPSs, in which the compartmentalization can be reversibly triggered by light irradiation[71]. For ATPSs composed of two or more types of stimuli-responsive polymers, the compartmentalization can be regulated by different physicochemical signals, creating opportunities in synthetic biology and biochemical engineering.

Methods

Materials and chemicals

The TR-ATPS was composed of self-synthesized PNIPAM and DEX (M_w = 500 kg/mol, Dieckmann). The synthesis of PNIPAM followed a standard radical polymerization process[72]. 1 g of NIPAM was dissolved in 10 ml water and oscillated for 10 mins to form a uniform solution. 5 mg of APS was added into the solution and sonicated for 2 min for complete dissolution. Subsequently, 10 µL TMEDA was injected into the above solution to initiate the reaction. After 24 h, the resulting solution was dialyzed for 72 h and freeze-dried for another 48 h. The obtained PNIPAM power was stored at 4 °C. PDEA was synthesized by the same method as PNIPAM using *N, N*-diethylacrylamide (TCI) as monomers. Two ATPSs, PNIPAM/polyacrylamide (PAM, M_n = 150 kg/mol, Sigma Aldrich) and DEX (M_w = 500 kg/mol, Dieckmann)/PEG (M_w = 3.5 kg/mol, Sigma Aldrich), were selected as controls. Rhodamine B labeled PNIPAM and PEG was custom-designed by Nanjing Starleaf Biological Technology CO., Ltd. Fluorescein isothiocyanate (FITC) was covalently attached to PAM (Nanjing Starleaf Biological Technology CO., Ltd) and DEX (TCI). SU-8 photoresist (2025) and SU-8 developer were bought from Micro-Chem. Polydimethylsiloxane (PDMS) microfluidic chips were prepared from PDMS prepolymer and curing agent (both from Dow Corning) following classic soft photolithography[73]. All reagents were used as received. Deionized (DI) water was used in all the experiments unless otherwise noted.

Compartmentalization of TR-ATPS

Different PNIPAM and DEX mass fractions were mixed and injected into a chamber for the following observation under a microscope. The chamber was prepared by sandwiching two coverslips with a spacer of 120 µm.

The PNIPAM (5 wt%)/DEX (5 wt%) system was prepared by adding 0.5 g PNIPAM and 0.5 g DEX in 9 mL DI water and then oscillated for 10 mins for complete dissolution. Thermo-responsive behaviors of the non-equilibrated droplets were observed under a microscope.

The prepared homogeneous PNIPAM (5 wt%)/DEX (5 wt%) system was centrifuged at 7168 × *g* for 30 mins and standing for 48 h to obtain the equilibrated PNIPAM-rich and DEX-rich phases. The PNIPAM-rich phase at the top and the dextran-rich phase at the bottom were then collected separately. Finally, the collected PNIPAM-rich and dextran-rich phases were injected into microfluidic chips as external and internal phases, respectively, for generating the all-aqueous double emulsions. The flow rate of the inner phase, external phase, and oil phase were 500, 500, and 5000 µL/h. The continuous flow was broken by an oil phase consisting of FC-40 with 1% fluorosurfactant (3 M), which stabilized the resulting emulsions. The resulting all-aqueous emulsions were injected into the above-mentioned chamber to avoid the evaporation of solvents. The thermo-induced phase separations were observed under a microscope.

Biomolecules storage in TR-ATPS

1 µL Cy-5 labeled BSA (2 mg/mL, Bioss), 1 µL FITC labeled PLL (2 mg/mL, Sigma-Aldrich), and 1 µL Fam-labeled single-stranded RNA homopolymer poly(rA) of 40 nt (2 mg/mL, IDT) were separately mixed with 9 µL aqueous solution containing 5 wt% PNIAPM and 5 wt% DEX under oscillation for 5 min. 8 µL of the obtained mixture solution was injected into a chamber for the following observation under a microscope at 25 °C and 35 °C.

Spatiotemporal regulation of biochemical reaction via interception of enzymes

1 µL rhodamine-labeled GOX (2 mg/mL, Ruixi Biotech Co. Ltd) and 1 µL FITC-labeled HRP (2 mg/mL, Ruixi Biotech Co. Ltd) were mixed with 48 µL aqueous solution containing 5 wt% PNIAPM and 5 wt% DEX under oscillation for 5 min. 8 µL of the obtained mixture solution was injected into a chamber for the following observation under a microscope.

Enzymatic activities of glucose oxidase were detected using the Amplex® Red Glucose/Glucose Oxidase Assay Kit (Thermo Fisher) at different temperatures. Reactions containing 50 µM Amplex® Red reagent, 0.1 U/mL HRP, 10 mM glucose, and the indicated amount of glucose oxidase in 50 mM sodium phosphate buffer, pH 7.4, were incubated for 30 minutes. Enzymatic activities of HRP were evaluated by the Amplex® Red Hydrogen Peroxide/Peroxidase Assay Kit (Thermo Fisher). Reactions containing 50 µM Amplex® Red reagent, 1 mM H_2O_2, and the indicated amount of HRP in 50 mM sodium phosphate buffer, pH 7.4, were incubated for 30 minutes.

The kinetic behaviors of GOX@HRP in different working solutions were investigated by monitoring the fluorescence of the oxidation product of Amplex Red in 1-min intervals while changing the concentration of substrate, glucose. The reaction rate is measured using the early linear region of the product concentration within the first 5 min. At the early stage of the reaction, the substrate concentration is high, and the binding of the enzyme to the substrate has not reached equilibrium. In this case, the initial reaction rate can be approximated as a linear change, to facilitate measurement and calculation[74,75]. The maximal reaction velocity (V_{max}) and the Michaelis–Menten constant (K_m) were obtained via Lineweaver-Burk plots of the double reciprocal of the Michaelis–Menten equation, $1/v = K_m/V_{max}(1/S + 1/K_m)$. v and S correspond to the initial velocity and substrate concentration, respectively. Reactions containing 0.5 µM Amplex® Red reagent, 1 mU/mL HRP, 10 mU/mL glucose oxidase, and the indicated amount of glucose in a 50 mM sodium phosphate buffer (pH 7.4), a 50 mM sodium phosphate buffer containing PEG (1 wt%)/DEX (9 wt%), and a 50 mM sodium phosphate buffer containing PNIPAM (5 wt%)/DEX (5 wt%), respectively, were incubated for 30 minutes.

Characterization

A fluorescence microscope (Nikon Ti2-E) recorded all microscopic images and movies. A confocal laser scanning microscope (Zeiss LSM 880) with Airyscan platform was applied to take confocal images and movies. The fluorescence intensity of resorufin and the transmittance of the PDEA solution were monitored by a molecular device (SpectraMax iD3). FRAP was performed on a Carl Zeiss LSM 880 microscope. A 561-nm laser bleached the PNIPAM droplet labeled with rhodamine at 100% power for 5 s. Post-bleaching images and fluorescence intensity in the bleached region were taken at 2% power of the 561-nm laser every 1 s. Rearrangement of hydrogen bond in the PNIPAM (5 wt%)/DEX (5 wt%) aqueous solution below and above the LCST of PNIPAM are recorded by ATR-FTIR spectroscopy (PerkinElmer UATR Two) in the range 400–4000 cm^{-1}. ^1H NMR spectra were recorded with Bruker Avance III 500 spectrometer using D_2O as the solvent. The partitioning fraction for both GOX and HRP, defined as the fluorescence intensity of each enzyme in the PNIPAM/DEX phase divided by its overall fluorescence intensity, was calculated from the fluorescence images by Image J.

Data availability

Data generated in this study are provided in the paper and/or the Supplementary Information. All data are also available from the corresponding author upon request. Source data are provided with this paper.

References

1. Carmo-Fonseca, M. The contribution of nuclear compartmentalization to gene regulation. *Cell* **108**, 513–521 (2002).
2. Tu, B. P., Kudlicki, A., Rowicka, M. & McKnight, S. L. Logic of the yeast metabolic cycle: temporal compartmentalization of cellular processes. *Science* **310**, 1152–1158 (2005).
3. Chen, A. H. & Silver, P. A. Designing biological compartmentalization. *Trends Cell Biol.* **22**, 662–670 (2012).

4. Zhao, H., Ibrahimova, V., Garanger, E. & Lecommandoux, S. Dynamic spatial formation and distribution of intrinsically disordered protein droplets in macromolecularly crowded protocells. *Angew. Chem. Int. Ed.* **59**, 11028–11036 (2020).
5. Agapakis, C. M., Boyle, P. M. & Silver, P. A. Natural strategies for the spatial optimization of metabolism in synthetic biology. *Nat. Chem. Biol.* **8**, 527–535 (2012).
6. Aguzzi, A. & Altmeyer, M. Phase separation: linking cellular compartmentalization to disease. *Trends Cell Biol.* **26**, 547–558 (2016).
7. Samir, P. et al. DDX3X acts as a live-or-die checkpoint in stressed cells by regulating NLRP3 inflammasome. *Nature* **573**, 590–594 (2019).
8. Huang, W. Y. C. et al. A molecular assembly phase transition and kinetic proofreading modulate Ras activation by SOS. *Science* **363**, 1098 (2019).
9. Shan, Z. et al. Basal condensation of Numb and Pon complex via phase transition during Drosophila neuroblast asymmetric division. *Nat. Commun.* **9**, 737 (2018).
10. Lafontaine, D. L. J., Riback, J. A., Bascetin, R. & Brangwynne, C. P. The nucleolus as a multiphase liquid condensate. *Nat. Rev. Mol. Cell Biol.* **22**, 165–182 (2021).
11. Molliex, A. et al. Phase separation by low complexity domains promotes stress granule assembly and drives pathological fibrillization. *Cell* **163**, 123–133 (2015).
12. Lyon, A. S., Peeples, W. B. & Rosen, M. K. A framework for understanding the functions of biomolecular condensates across scales. *Nat. Rev. Mol. Cell Biol.* **22**, 215–235 (2021).
13. Alberti, S., Gladfelter, A. & Mittag, T. Considerations and challenges in studying liquid-liquid phase separation and biomolecular condensates. *Cell* **176**, 419–434 (2019).
14. Banani, S. F., Lee, H. O., Hyman, A. A. & Rosen, M. K. Biomolecular condensates: organizers of cellular biochemistry. *Nat. Rev. Mol. Cell Biol.* **18**, 285–298 (2017).
15. Phair, R. D. & Misteli, T. High mobility of proteins in the mammalian cell nucleus. *Nature* **404**, 604–609 (2000).
16. Weidtkamp-Peters, S. et al. Dynamics of component exchange at PML nuclear bodies. *J. Cell Sci.* **121**, 2731–2743 (2008).
17. Li, J. et al. Programmable spatial organization of liquid-phase condensations. *Chem* **8**, 784–800 (2022).
18. Kilgore, H. R. & Young, R. A. Learning the chemical grammar of biomolecular condensates. *Nat. Chem. Biol.* **18**, 1298–1306 (2022).
19. Brangwynne, C. P., Mitchison, T. J. & Hyman, A. A. Active liquid-like behavior of nucleoli determines their size and shape in Xenopus laevis oocytes. *Proc. Natl Acad. Sci.* **108**, 4334 (2011).
20. Brangwynne, C. P. et al. Germline P granules are liquid droplets that localize by controlled dissolution/condensation. *Science* **324**, 1729 (2009).
21. Alberti, S. & Hyman, A. A. Biomolecular condensates at the nexus of cellular stress, protein aggregation disease and ageing. *Nat. Rev. Mol. Cell Biol.* **22**, 196–213 (2021).
22. Wang, Y. et al. Hierarchically compartmentalized supramolecular gels through multilevel self-sorting. *J. Am. Chem. Soc.* **141**, 2847–2851 (2019).
23. Xu, C., Martin, N., Li, M. & Mann, S. Living material assembly of bacteriogenic protocells. *Nature* **609**, 1029–1037 (2022).
24. Mason, A. F., Buddingh, B. C., Williams, D. S. & van Hest, J. C. M. Hierarchical self-assembly of a copolymer-stabilized coacervate protocell. *J. Am. Chem. Soc.* **139**, 17309–17312 (2017).
25. Buddingh, B. C. & van Hest, J. C. M. Artificial cells: synthetic compartments with life-like functionality and adaptivity. *Acc. Chem. Res.* **50**, 769–777 (2017).
26. Zhang, M. et al. Pickering emulsion droplet-based biomimetic microreactors for continuous flow cascade reactions. *Nat. Commun.* **13**, 475 (2022).
27. Chao, Y. & Shum, H. C. Emerging aqueous two-phase systems: from fundamentals of interfaces to biomedical applications. *Chem. Soc. Rev.* **49**, 114–142 (2020).
28. Li, C. et al. One-pot self-assembly of dual-color domes using monosized silica nanoparticles. *Nano Lett.* **22**, 5236–5243 (2022).
29. Lo, H. Y. et al. Diffusion-dominated pinch-off of ultralow surface tension fluids. *Phys. Rev. Lett.* **123**, 134501 (2019).
30. Song, Y. et al. Fabrication of fibrillosomes from droplets stabilized by protein nanofibrils at all-aqueous interfaces. *Nat. Commun.* **7**, 12934 (2016).
31. Song, Y. et al. Budding-like division of all-aqueous emulsion droplets modulated by networks of protein nanofibrils. *Nat. Commun.* **9**, 2110 (2018).
32. Chao, Y., Mak, S. Y., Rahman, S., Zhu, S. & Shum, H. C. Generation of high-order all-aqueous emulsion drops by osmosis-driven phase separation. *Small* **14**, 1802107 (2018).
33. Liu, S. et al. Enzyme-mediated nitric oxide production in vasoactive erythrocyte membrane-enclosed coacervate protocells. *Nat. Chem.* **12**, 1165–1173 (2020).
34. Xie, G. et al. Compartmentalized, all-aqueous flow-through-coordinated reaction systems. *Chem* **5**, 2678–2690 (2019).
35. Zhu, S. et al. Rapid multilevel compartmentalization of stable all-aqueous blastosomes by interfacial aqueous-phase separation. *ACS Nano* **14**, 11215–11224 (2020).
36. Guo, W. et al. Non-associative phase separation in an evaporating droplet as a model for prebiotic compartmentalization. *Nat. Commun.* **12**, 3194 (2021).
37. Strulson, C. A., Molden, R. C., Keating, C. D. & Bevilacqua, P. C. RNA catalysis through compartmentalization. *Nat. Chem.* **4**, 941–946 (2012).
38. Chen, Y. et al. Resolving optical and catalytic activities in thermoresponsive nanoparticles by permanent ligation with temperature-sensitive polymers. *Angew. Chem. Int. Ed.* **58**, 11910–11917 (2019).
39. Zhang, P. et al. A microstructured graphene/poly(n-isopropylacrylamide) membrane for intelligent solar water evaporation. *Angew. Chem. Int. Ed.* **57**, 16343–16347 (2018).
40. Fernández-Castaño Romera, M. et al. Mimicking active biopolymer networks with a synthetic hydrogel. *J. Am. Chem. Soc.* **141**, 1989–1997 (2019).
41. Du, X. et al. Photothermally triggered shape-adaptable 3d flexible electronics. *Adv. Mater. Technol.* **2**, 1700120 (2017).
42. Du, X. et al. Reconfiguration, camouflage, and color-shifting for bioinspired adaptive hydrogel-based millirobots. *Adv. Funct. Mater.* **30**, 1909202 (2020).
43. Marguet, M., Bonduelle, C. & Lecommandoux, S. Multicompartmentalized polymeric systems: towards biomimetic cellular structure and function. *Chem. Soc. Rev.* **42**, 512–529 (2013).
44. Abbas, M., Lipiński, W. P., Wang, J. & Spruijt, E. Peptide-based coacervates as biomimetic protocells. *Chem. Soc. Rev.* **50**, 3690–3705 (2021).
45. Zhang, L. et al. One-step microfluidic fabrication of polyelectrolyte microcapsules in aqueous conditions for protein release. *Angew. Chem. Int. Ed.* **55**, 13470–13474 (2016).
46. Ma, Q., Song, Y., Kim, J. W., Choi, H. S. & Shum, H. C. Affinity partitioning-induced self-assembly in aqueous two-phase systems: templating for polyelectrolyte microcapsules. *ACS Macro Lett.* **5**, 666–670 (2016).
47. Karimi, M. et al. Smart micro/nanoparticles in stimulus-responsive drug/gene delivery systems. *Chem. Soc. Rev.* **45**, 1457–1501 (2016).

48. Cui, H. et al. Dynamic assembly of viscoelastic networks by aqueous liquid–liquid phase separation and liquid–solid phase separation (AqLL-LS PS2). *Adv. Mater.* **34**, 2205649 (2022).
49. Tamai, Y., Tanaka, H. & Nakanishi, K. Molecular dynamics study of polymer–water interaction in hydrogels. 1. Hydrogen-bond structure. *Macromolecules* **29**, 6750–6760 (1996).
50. Hu, Y. et al. Hydrophilicity-hydrophobicity transformation, thermoresponsive morphomechanics, and crack multifurcation revealed by AIEgens in mechanically strong hydrogels. *Adv. Mater.* **33**, 2101500 (2021).
51. Wang, J., Lin, L., Cheng, Q. & Jiang, L. A strong bio-inspired layered PNIPAM–clay nanocomposite hydrogel. *Angew. Chem. Int. Ed.* **51**, 4676–4680 (2012).
52. De Vito, F., Veytsman, B., Painter, P. & Kokini, J. L. Simulation of the effect of hydrogen bonds on water activity of glucose and dextran using the Veytsman model. *Carbohydr. Polym.* **117**, 236–246 (2015).
53. Guo, L., Sato, H., Hashimoto, T. & Ozaki, Y. FTIR study on hydrogen-bonding interactions in biodegradable polymer blends of Poly(3-hydroxybutyrate) and poly(4-vinylphenol). *Macromolecules* **43**, 3897–3902 (2010).
54. Coleman, M. M., Skrovanek, D. J., Hu, J. & Painter, P. C. Hydrogen bonding in polymer blends. 1. FTIR studies of urethane-ether blends. *Macromolecules* **21**, 59–65 (1988).
55. Martinez-Moro, M., Jenczyk, J., Giussi, J. M., Jurga, S. & Moya, S. E. Kinetics of the thermal response of poly(N-isopropylacrylamide co methacrylic acid) hydrogel microparticles under different environmental stimuli: a time-lapse NMR study. *J. Colloid Interface Sci.* **580**, 439–448 (2020).
56. Tan, H. et al. Heterogeneous multi-compartmental hydrogel particles as synthetic cells for incompatible tandem reactions. *Nat. Commun.* **8**, 663 (2017).
57. Madadlou, A., Saggiomo, V., Schroën, K. & Fogliano, V. All-aqueous emulsions as miniaturized chemical reactors in the food and bioprocess technology. *Curr. Opin. Food Sci.* **33**, 165–172 (2020).
58. Zhao, H. et al. Spatiotemporal dynamic assembly/disassembly of organelle-mimics based on intrinsically disordered protein-polymer conjugates. *Adv. Sci.* **8**, 2102508 (2021).
59. Lin, H. & Cornish, V. W. Screening and selection methods for large-scale analysis of protein function. *Angew. Chem. Int. Ed.* **41**, 4402–4425 (2002).
60. Kohen, A. & Klinman, J. P. Enzyme catalysis: beyond classical paradigms. *Acc. Chem. Res.* **31**, 397–404 (1998).
61. Tan, C., Saurabh, S., Bruchez, M. P., Schwartz, R. & LeDuc, P. Molecular crowding shapes gene expression in synthetic cellular nanosystems. *Nat. Nanotechnol.* **8**, 602–608 (2013).
62. Pavlovic, M. et al. Cascade kinetics in an enzyme-loaded aqueous two-phase system. *Langmuir* **36**, 1401–1408 (2020).
63. Dewey, D. C., Strulson, C. A., Cacace, D. N., Bevilacqua, P. C. & Keating, C. D. Bioreactor droplets from liposome-stabilized all-aqueous emulsions. *Nat. Commun.* **5**, 4670 (2014).
64. Wang, C., Zhang, Z., Wang, Q., Wang, J. & Shang, L. Aqueous two-phase emulsions toward biologically relevant applications. *Trends Chem.* **5**, 61–75 (2023).
65. Roy, D., Brooks, W. L. A. & Sumerlin, B. S. New directions in thermoresponsive polymers. *Chem. Soc. Rev.* **42**, 7214–7243 (2013).
66. Maeda, Y., Nakamura, T. & Ikeda, I. Hydration and phase behavior of poly(n-vinylcaprolactam) and poly(n-vinylpyrrolidone) in water. *Macromolecules* **35**, 217–222 (2002).
67. Lessard, D. G., Ousalem, M., Zhu, X. X., Eisenberg, A. & Carreau, P. J. Study of the phase transition of poly(N,N-diethylacrylamide) in water by rheology and dynamic light scattering. *J. Polym. Sci. Part B: Polym. Phys.* **41**, 1627–1637 (2003).
68. Bayliss, N., Yilmaz, G., Plucinski, A., Becer, C. R. & Schmidt, B. V. K. J. Thermoresponsive behaviour of poly(N,N-diethylacrylamide) in aqueous two-phase systems. *Polym. Chem.* **14**, 4101–4108 (2023).
69. Liu, F. & Urban, M. W. Recent advances and challenges in designing stimuli-responsive polymers. *Prog. Polym. Sci.* **35**, 3–23 (2010).
70. Zhang, N., Salzinger, S. & Rieger, B. Poly(vinylphosphonate)s with widely tunable LCST: a promising alternative to conventional thermoresponsive polymers. *Macromolecules* **45**, 9751–9758 (2012).
71. Tang, Y. et al. Up/down tuning of poly(ionic liquid)s in aqueous two-phase systems. *Angew. Chem. Int. Ed.* **62**, e202215722 (2023).
72. Wang, C., Flynn, N. T. & Langer, R. Controlled structure and properties of thermoresponsive nanoparticle–hydrogel composites. *Adv. Mater.* **16**, 1074–1079 (2004).
73. Nan, L., Cao, Y., Yuan, S. & Shum, H. C. Oil-mediated high-throughput generation and sorting of water-in-water droplets. *Microsyst. Nanoeng.* **6**, 70 (2020).
74. Markin, C. J. et al. Revealing enzyme functional architecture via high-throughput microfluidic enzyme kinetics. *Science* **373**, eabf8761 (2021).
75. Wolfenden, R. & Snider, M. J. The depth of chemical time and the power of enzymes as catalysts. *Acc. Chem. Res.* **34**, 938–945 (2001).

Acknowledgements

H.C. acknowledges the financial support provided by the National Natural Science Foundation of China (No. 52003287). Y.Z. acknowledges the financial support provided by the National Natural Science Foundation of China (No. 2302128), Guangdong Basic and Applied Basic Research Foundation (No. 2024A1515010990), Shenzhen Science and Technology Program (RCBS20231211090713027), and Medicine Plus Program of Shenzhen University (2024YG015). H.C.S. acknowledges the financial support provided by the National Natural Science Foundation of China (NSFC)/Research Grants Council of Hong Kong (RGC) Joint Research Scheme (No. N_HKU718/19), General Research Fund (Nos. 17317322, 17306221, and 17306820), Collaborative Research Fund (C7165-20GF), from RGC. Y.Z., Y.L., H.L., S.H., and H.C.S. were partly supported by the Health@InnoHK Programme under the Innovation and Technology Commission of the Hong Kong SAR Government. The authors acknowledge the technical support from the Centre for PanorOmic Sciences, HKU Li Ka Shing Faculty of Medicine. The authors thank Dr. Han Han from Prof. Sir Fraser Stoddart's group at HKU for the ^{1}H NMR characterization and analysis. The authors thank Dr. Yang Song and Dr. Wei Guo for the helpful discussions.

Author contributions

H.C. conceived the idea and designed the experiments. H.C. conducted the experiments, analyzed the results, and wrote the manuscript. H.C.S. supervised the study, analyzed the results, and revised the manuscript. S.L. and H.C. drew the schematic diagrams. Y.C. designed and fabricated the microfluidic chips. Y.Z., Q.M., Y.L., H.L., C.L., Y.X., and S.H. contributed to the discussion and reviewed the manuscript.

Competing interests

H.C.S. is a scientific advisor of EN Technology Limited, MicroDiagnostics Limited and Upgrade Biopolymers Limited in which he owns some equity, and also a managing director of the research center, namely Advanced Biomedical Instrumentation Center Limited. The works in the paper are however not directly related to the works of these entities. The remaining authors declare no competing interests.

Additional information

Supplementary information The online version contains supplementary material available at https://doi.org/10.1038/s41467-024-51043-z.

Correspondence and requests for materials should be addressed to Ho Cheung Shum.

Peer review information *Nature Communications* thanks Jianbo Liu, Bernhard Schmidt and the other, anonymous, reviewer for their contribution to the peer review of this work. A peer review file is available.